

# UC San Diego

## UC San Diego Previously Published Works

### Title

Hydrodynamic influences on acoustical and optical backscatter in a fringing reef environment

### Permalink

<https://escholarship.org/uc/item/4tv708wz>

### Journal

Journal of Geophysical Research - Oceans, 122(1)

### ISSN

2169-9275

### Authors

Pawlak, Geno  
Moline, Mark A  
Terrill, Eric J  
[et al.](#)

### Publication Date

2017

### DOI


10.1002/2016jc012497

Peer reviewed

## RESEARCH ARTICLE

10.1002/2016JC012497

## Hydrodynamic influences on acoustical and optical backscatter in a fringing reef environment

Geno Pawlak <sup>1</sup>, Mark A. Moline<sup>2</sup>, Eric J. Terrill<sup>3</sup>, and Patrick L. Colin<sup>4</sup>

## Key Points:

- Optical and high-frequency acoustic backscatter is strongly linked to wave and tidal forcing for a tropical forereef
- Changes in properties indicate relative increases in smaller particles with increasing wave forcing
- Variations in modeled reflectance spectra indicate particles are consistent with whitening events

## Correspondence to:

G. Pawlak,  
pawlak@ucsd.edu

## Citation:

Pawlak, G., M. A. Moline, E. J. Terrill, and P. L. Colin (2017), Hydrodynamic influences on acoustical and optical backscatter in a fringing reef environment, *J. Geophys. Res. Oceans*, 122, 322–335, doi:10.1002/2016JC012497.

Received 31 MAR 2016

Accepted 11 DEC 2016

Accepted article online 22 DEC 2016

Published online 20 JAN 2017

<sup>1</sup>Department of Mechanical and Aerospace Engineering, University of California San Diego, La Jolla, California, USA,<sup>2</sup>School of Marine Science and Policy, College of Earth, Ocean, and Environment, University of Delaware, Lewes, Delaware, USA, <sup>3</sup>Laboratory, Scripps Institution of Oceanography, University of California San Diego, La Jolla, California, USA, <sup>4</sup>Coral Reef Research Foundation, Koror, Palau

**Abstract** Observations of hydrodynamics along with optical and acoustical water characteristics in a tropical fringing reef environment reveal a distinct signature associated with flow characteristics and tidal conditions. Flow conditions are dominated by tidal forcing with an offshore component from the reef flat during ebb. Measurements span variable wave conditions enabling identification of wave effects on optical and acoustical water properties. High-frequency acoustic backscatter (6 MHz) is strongly correlated with tidal forcing increasing with offshore directed flow and modulated by wave height, indicating dominant hydrodynamic influence. Backscatter at 300 and 1200 kHz is predominantly diurnal suggesting a biological component. Optical backscatter is closely correlated with high-frequency acoustic backscatter across the range of study conditions. Acoustic backscatter frequency dependence is used along with changes in optical properties to interpret particle-size variations. Changes across wave heights suggest shifts in particle-size distributions with increases in relative concentrations of smaller particles for larger wave conditions. Establishing a connection between the physical processes of a fringing tropical reef and the resulting acoustical and optical signals allows for interpretation and forecasting of the remote sensing response of these phenomena over larger scales.

## 1. Introduction

Tropical reefs are generally characterized by high acoustical and optical water clarity as a result of low suspended sediment and nutrient inputs along with low water column productivity. Sediment loading in reef environments can vary significantly in time and space, however, in response to regular or episodic forcing from tides, wind, swell, and rainfall, with implications for reef health [Fortes, 2000; Weber *et al.*, 2012]. In addition, these forcing mechanisms vary in relative contributions across the range of reef morphologies extending from the forereef to lagoonal environments and tropical river mouths. Previous studies have noted high spatial and temporal variability in optical backscatter and sediment concentrations for subsets of reef environments [Storlazzi and Jaffe, 2008; Storlazzi *et al.*, 2009; Blondeau-Patissier *et al.*, 2009]. Larcombe *et al.* [1995] identified wave forcing as the primary mechanism for turbidity generation for portions of the Great Barrier Reef, where suspended sediments are predominantly of terrigenous origins. Morimoto *et al.* [2010] also identified resuspension due to surface waves as the dominant forcing for turbidity variations along a cross-reef transect in southwestern Japan and noted an accompanying biological response due to increased nutrients. Observations in a reef lagoon by Jouon *et al.* [2008] indicated high spatiotemporal variability in particle concentrations and size distributions. Biological aggregation was also significant, particularly near coral regions and when concentrations were low.

In addition to their relevance for benthic ecology, optical properties can also have effects on reef circulation. The high radiative surface heat fluxes that are characteristic for tropical environments create cross-isobath baroclinic gradients that, in turn, drive diurnal exchange flows [Monismith *et al.*, 2006; Molina *et al.*, 2014]. Given generally high water clarity, in shallow water a significant fraction of the incident shortwave radiation can reach the bottom. Wells *et al.* [2012] reported the occurrence of near-bed thermal inversions on a tropical forereef on 20% of days over a 2 year period. The net effect of heating on stratification, and thus on the baroclinic exchange, depends on the depth over which the incident radiation is absorbed, and thus also on optical properties of the water column.

Variations in optical water properties also have important implications for remote sensing applications including mapping of benthic habitats [Holden and LeDrew, 2002; Mishra et al., 2006; Minghelli-Roman and Dupouy, 2014] and bathymetry [Stumpf et al., 2003]. Conversely, remotely sensed variations in optical water properties enable assessment and monitoring of physical processes and climatological variables [Mumby et al., 2004; Gove et al., 2013; Hedley et al., 2016].

Inclusion of optical approaches to quantify the physical dynamics in and around coral reefs and atolls has been used for some time [Storlazzi et al., 2004; Presto et al., 2006]. Evaluating optical variability can be useful to identify and quantify the processes that influence the complex flows, sources of particulate, and dissolved material and distributions of optical constituents in these areas [Storlazzi and Jaffe, 2008]. These optical constituents, in turn, allow for quantification of the direct effects on remotely sensing these environments as shown by Holden and LeDrew [2002]. Ultimately, the challenge is in translating remote sensing variables into usable products, such as bottom substrate, water clarity, and flow conditions. It is therefore important to connect the distributions of optical constituents to the physical processes as well as to resolve the spatial and temporal influences of optical quantities on deriving these processes from remotely sensed data.

Here we address this challenge using analysis of concomitant optical and acoustical observations in a tropical forereef environment, examining their variations with changes in tidal flow and wave forcing. These variations are used to infer characteristics and sources of suspended particle-size distributions across the hydrodynamic regimes. We further examine the implications of water property changes on remote sensing reflectance to illustrate how physical processes affect remotely sensed data in space and time.

## 2. Observations

Observations were carried out at Ngederrak Reef (Figure 1) along the eastern coast of the Palauan barrier reef complex in March 2012, as part of a larger field campaign targeting reef circulation. The narrow forereef shelf slopes seaward at about 7% between the 5 and 20 m isobaths, after which the depth drops off sharply to depths of about 75 m. The shelf is slightly narrower to the southwest, but is otherwise relatively uniform over this region. In the onshore direction, the bathymetry slopes up sharply to the reef flat, where depths are relatively uniform at 1–2 m with deeper regions in the back reef. Ngederrak Reef is bordered to the north by the Ngel Channel and to the south by the Lighthouse Channel.

The forereef substrate is comprised of dense staghorn coral (*Acroporida sp.*) beds interspersed with regions of sandy coral rubble and sporadic large (1–5 m) coral bommies. The reef flat is comprised of a matrix of seagrass beds (*Enhalus acoroides*, *Halodule sp.*, and *Thalassia hemprichii*), sand bottom, and coral beds [Colin, 2009]. Although the cross-shore structure at Ngederrak Reef is similar to that of a barrier reef, it is not a true barrier reef since it is bordered by a sunken barrier complex 2–3 km offshore with depths of 3–12 m [Colin, 2009].

The data described here were obtained at three locations along a cross-shore transect on the forereef. An upward-looking 1200 kHz RDInstruments acoustic Doppler current profiler (ADCP) was deployed on the bed at a depth of approximately 9 m. The ADCP uses four acoustic beams to obtain vertical profiles for three velocity components in 0.25 m bins over the water column. Velocities and acoustic echo intensities were recorded for individual pings at 1 Hz for each bin. In addition, the ADCP measured pressure and temperature at the bed. A mooring located nearby at the same isobath included temperature measurements at 1 m intervals from the bed to 1 m below the surface. A 300 kHz RDInstruments ADCP was deployed roughly 100 m offshore of the 9 m ADCP at a mean depth of 17.5 m. Velocity and echo intensity profiles were recorded at 1 Hz with 1 m vertical bins. As for the shallow ADCP, a nearby mooring measured temperature at 1–1.5 m vertical intervals to 1 m below the surface.

A set of three 6 MHz Nortek Vector acoustic Doppler velocimeters (ADV) was deployed along on a 3 m vertical spar on a small sand/rubble patch. Each ADV measured three velocity components and acoustic echo intensity within a 1 cm<sup>3</sup> volume at 16 Hz. One ADV measurement volume was located at approximately 3 mab (meters above the bed) with two others located at approximately 1.5 mab, offset horizontally from each other.

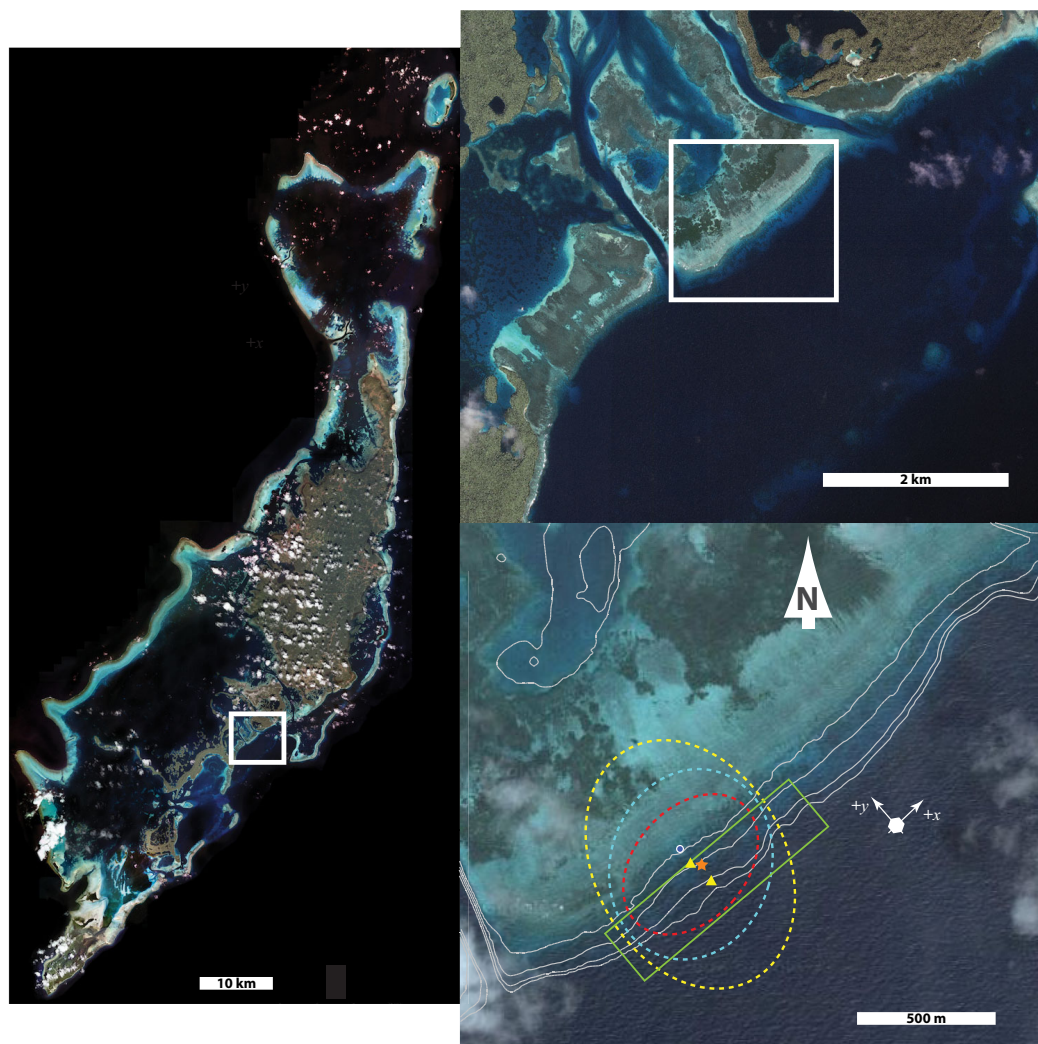


**Figure 1.** Satellite view of Republic of Palau with close-up of (top right) Ngederrak Reef region and (bottom right) study site. Yellow triangles indicate location of 1200 and 300 kHz ADCPs, with orange star denoting location of ADV and optics stacks. Yellow, cyan, and red-dashed ellipses indicate current ellipses at 1.3, 3.8, and 6.3 m depths, respectively. The size of the ellipses indicates the approximate tidal excursion over an  $M_2$  tidal period (12.42 h). Isobaths in lower right are at 5, 10, 15, and 20 m.

A second vertical spar, located about 5 m alongshore from the ADV spar, included a Wetlabs ac-9 spectrophotometer and a Wetlabs VSF-3 optical scattering sensor with measurements obtained at about 2 mab. These two instruments were used to measure the inherent optical properties of the water (independent of incident solar light field and associated angular considerations). The ac-9 spectrophotometer measures light absorption,  $a$ , and attenuation,  $c$ , at 9 wavelengths between 412 and 715 nm, using a pumped flow-through system. Measurements of  $a$  and  $c$  coefficients were made at 6 Hz. Before use of coefficients, ac-9 data were processed for temperature and salinity effects according to Pegau *et al.* [1997], for scattering artifacts according to Zaneveld *et al.* [1994], and for instrument drifts since the last manufacturer's calibration, determined using pure water calibrations according to Twardowski *et al.* [1999]. The VSF-3 measures optical scattering at three wavelengths (470, 532, and 650 nm) and at three angles (100, 125, and 150 degrees) in order to estimate the volume scattering function (VSF) [Moore *et al.* 2000]. Both instruments were factory calibrated prior to deployment.

The ADV spar and the ADCPs were deployed over a 9 day window, 16–25 March, 2012 (Figure 2). The optical data were obtained in two shorter spans, 17–20 March and 23 and 24 March (Figures 2g and 2h). The measurements spanned two distinct forcing regimes including a period of strong easterly winds with low solar forcing and tropical rain storms, which extended through 18 March, followed by a period of strong solar forcing and light winds.

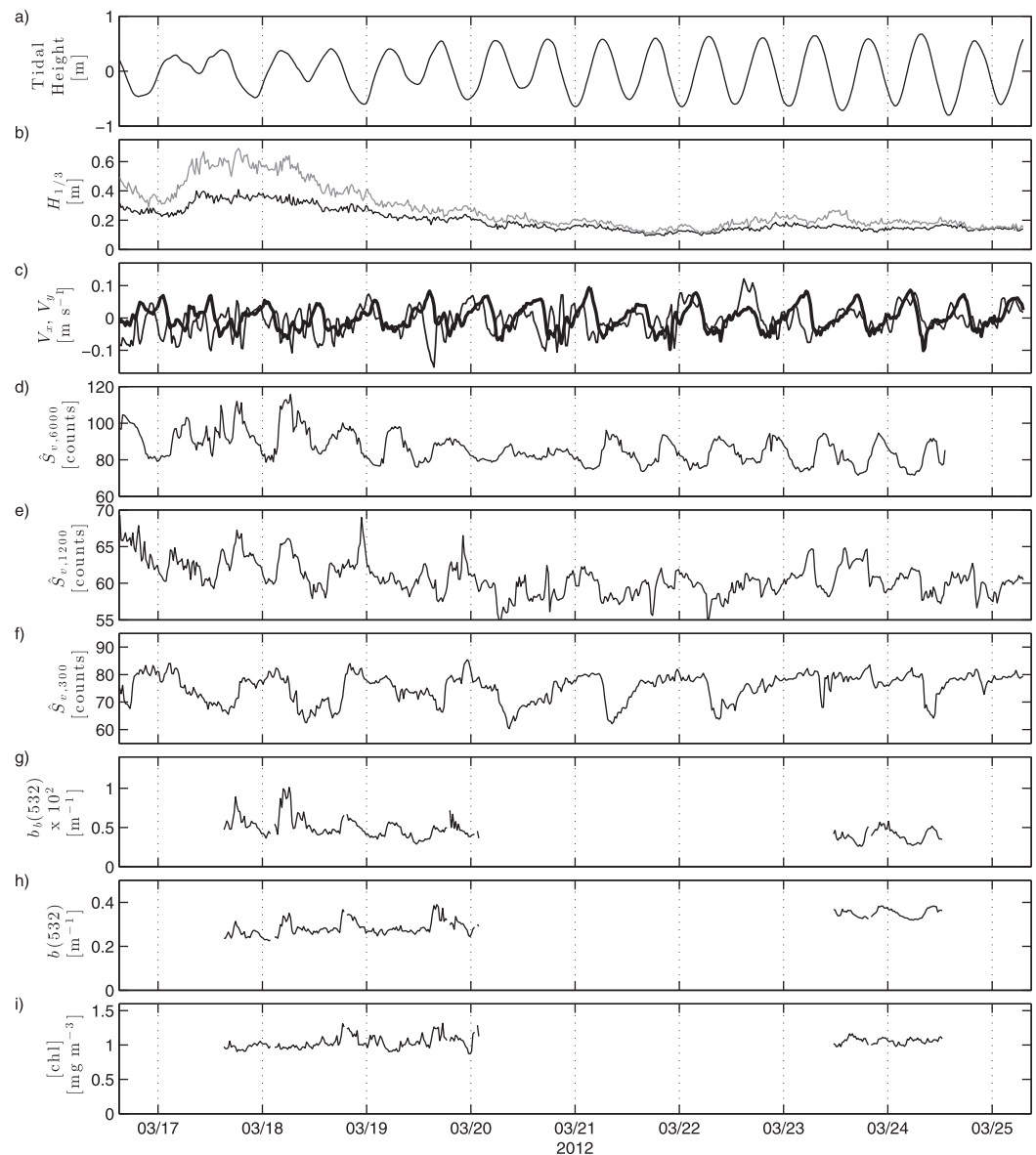


**Figure 2.** Observational data for study period (local time). (a) tidal height, (b) significant wave height from zero-crossing (black) and spectral (gray) methods; (c) along-shore (thin black) and cross-shore (thick black) depth averaged velocity; (d) 6 MHz acoustic backscatter; (e) 1200 kHz acoustic backscatter; (f) 300 kHz acoustic backscatter; (g) optical backscatter (532 nm) at 117°; (h) total optical scattering (b: 532 nm); and (i) chlorophyll-a concentration.

Tidal variation, obtained from pressure measurements at the 9 m ADCP, averaged over 20 min intervals, is shown in Figure 2a. Significant wave height  $H_{1/3}$  is estimated from the 9 m ADCP 1 Hz pressure data using a zero-crossing analysis, as an average of the 1/3rd highest waves within each 20 min interval (Figure 2d). Wave heights were elevated over the first few days of the study coincident with increased easterly wind forcing. Wave periods, estimated from the zero-crossing analysis, ranged between 5 s during the high wind period to 10 s during calm winds. From in situ visual observations, breaking waves were observed on the reef crest with whitecapping offshore on 17 and 18 March. Temperature and salinity data (not shown), obtained from a bottom mounted Seabird 37 near the 9 m ADCP location, were relatively constant over the study period. Temperature showed a slow increase of about 0.5°C along with weak variations on diurnal timescales (~0.4°C). Salinity showed weak variations ( $\sigma=0.03$  psu) over the observational window following a small drop (~0.1 psu) on 17 March coincident with the increase in waves and wind speed, likely associated with vertical mixing of surface precipitation.



Current velocities were defined using 20 min averages within each ADCP depth bin. Velocities were rotated into cross and along-shore components ( $V_y$ ,  $V_x$ ) based on the local isobaths which are oriented at approximately +50 degrees from east (see Figure 1). The current regime was complex at the site, but was dominantly tidally driven (Figure 2c). The depth-averaged alongshore flow component at the 9 m site had magnitudes of up to  $10 \text{ cm s}^{-1}$  and was generally positive (toward the NE) with the rising tide, turning to the SE on the ebb with a slight phase lead relative to the tidal height. Significant oscillations with periods of 1–2 h were observed in the along-shore flow, which may be associated with pulsing outflow jets in the channels to the north and south. The cross-shore flow had similar amplitudes ( $\pm 10 \text{ cm s}^{-1}$ ), with flow in the onshore direction during the flood tide corresponding to flow over the reef flat and into the lagoon. Tidal excursions were on the order of  $\pm 0.5 \text{ km}$  in both the along and cross-shore directions. Mean along and cross-shore velocities over the study period were  $-0.8 \text{ cm s}^{-1}$  (to the southwest) and  $0.3 \text{ cm s}^{-1}$  (onshore), respectively. The outflow phase for the cross-shore flow typically began with depth uniform flow but quickly became surface intensified with a weak return flow near the bed, indicative of a strong outflow jet off of the shallow reef flat. The tidal ellipses for the 9 m ADCP in Figure 1 reflect the complex structure of the flows, with the near surface velocities primarily oriented in the cross-shore direction and the near-bed flow oriented in the along-shore direction. The ellipses also highlight the vertical flow structure with higher amplitudes near the surface. Velocities measured by the 300 kHz ADCP at the 17.5 m isobath were qualitatively similar to those at 9 m. ADV velocities correlated well ( $R^2=0.8$  for  $V_y$ ,  $R^2=0.87$  for  $V_x$ ) with 9 m ADCP measurements at 2 m above the bed.

As noted, the cross-shore flow is dominantly tidal (Figure 2c) and wave effects on circulation are weak due to relatively small wave heights during the study period. Similarly, wave-driven Lagrangian flow (Stokes drift) is estimated to be negligible ( $<1 \text{ cm s}^{-1}$ ) based on the observed wave heights and periods.

### 2.1. Optical and Acoustical Properties

Acoustic backscatter was estimated from the ADCP echo amplitude data following the methods described by Deines [1999] [see also Sevadjian *et al.*, 2010]. Absolute measurements of acoustic backscatter require careful ADCP calibration. Here, our interest is in examining the relative variations in acoustic backscatter so calibrations for the electronic constants were not necessary. Echo amplitude ( $E_A$ ) is recorded within each bin along each of the four beams in arbitrary units that are proportional to the logarithm of the echo power. Data are obtained at 1 Hz as for the velocity measurements described earlier and then averaged over 20 min intervals matching the velocity processing.

Following Deines [1999], the acoustic volume backscattering coefficient,  $S_v$ , is calculated from the basic sonar equation as:

$$S_v = \hat{C} + [20 \log_{10} R - 2\alpha R] + K_c E_A + 10 \log_{10} T \quad (1)$$

where  $\hat{C}$  is a calibration constant that is determined by the system-specific acoustic characteristics (transmit power, pulse length, transducer characteristics, etc.). The term in brackets represents the variations due to beam spreading and to attenuation where  $R$  is the along-beam range (m) and  $\alpha$  is the frequency-dependent absorption coefficient ( $\text{dB m}^{-1}$ ). We use the standard value of  $K_c = 0.45 \text{ dB m}^{-1}$  for the echo intensity-scale factor [Deines, 1999]. The final term represents the variation in the acoustic backscatter due to temperature changes. For the small temperature variations measured here, this contribution results in changes in backscatter of less than 1%, so this is neglected in our analysis. The relative variation in acoustic intensity, corrected for range and neglecting temperature changes, is given then as:

$$\hat{S}_v = S_v - \hat{C} = [20 \log_{10} R - 2\alpha R] + K_c E_A \quad (2)$$

Relative acoustic backscatter is calculated using the 300 and the 1200 kHz ADCP data for each depth bin using equation (2). Relative acoustic backscatter at 6 MHz is obtained directly from the echo amplitude reported by the ADVs. Since the ADV data represent measurements within a single, small ( $\sim 1 \text{ cm}^3$ ) control volume, no range correction is required. Because all acoustic measurements are uncalibrated, the values are given as “counts” relative to an arbitrary constant that differs for each instrument.

Acoustic backscatter intensity responds differently to particle sizes as a function of acoustic wavelength. For solid particles whose diameter,  $d$ , is comparable to or larger than the acoustic wavelength so that  $kd > 1$ , where  $k$  is the wavenumber, the acoustic backscatter at a given frequency is proportional to particle

geometric cross section [Hay, 1991; Medwin and Clay, 1997] so that backscatter per unit volume varies as  $(kd)^{-1}$ . For the acoustic frequencies of 300, 1200, and 6 MHz considered here,  $kd = 1$  (the nondimensional value at which geometric scatter is the dominant mechanism) corresponds to scatterers of roughly 800, 200, and 40  $\mu\text{m}$ , respectively. For smaller particles, where  $kd < 1$ , Rayleigh scattering is dominant and backscatter per unit volume drops off rapidly as  $(kd)^3$  [Medwin and Clay, 1997; Lynch et al., 1997].

Total optical backscattering coefficient,  $b_b$ , is calculated from the volume scattering function  $\beta(\theta)$  using

$$b_b = 2\pi \int_{\pi/2}^{\pi} \beta(\theta) \sin\theta d\theta \quad (3)$$

where  $\theta$  is the scattering angle and  $\beta(\theta)$  is estimated by fitting a third-order polynomial to the three values measured by the VSF-3 along with a fourth value of zero at  $\theta = \pi$ . Total optical scattering  $b$ , which includes the forward scattering component, is calculated using the ac-9 measurements via the difference between absorption  $a$  and attenuation  $c$ . Chlorophyll-a concentration [ $chl$ ] is estimated using absorption data from the ac-9 measurements following the chlorophyll absorption line height method [Davis et al., 1997; Boss et al., 2007; Whitmire et al., 2007].

Time series for acoustic and optical properties are shown in Figures 2d–2i. ADCP acoustic backscatter (ABS) at 300 kHz ( $\hat{S}_{v,600}$ ) and 1200 kHz ( $\hat{S}_{v,1200}$ ), here represent depth-averaged data, excluding the near-surface values (15% of the depth) that are contaminated due to side lobe reflection. The 6 MHz ADV observations  $\hat{S}_{v,6000}$  represent variations from the upper ADV at 3 m above the bed. Both  $\hat{S}_{v,1200}$  and  $\hat{S}_{v,6000}$  show a decrease over the 9 day window, but variability at all three frequencies is dominated by changes over relatively short timescales. Optical properties also show variability at timescales less than a day during the two observational windows with a slight decrease in  $b_b$  and a corresponding small increase in  $b$  between the two time windows, matching the slope during the first deployment. Chlorophyll (Figure 2i) is relatively consistent around 1  $\text{mg}/\text{m}^3$ .

### 3. Physical Controls on Optical and Acoustical Variability

We examine the variability in water properties at diurnal and tidal timescales by ensemble averaging the observations by time of day and tidal phase. Figure 3 shows average diurnal and tidal variations in acoustic backscatter for the three measured frequencies. Here tidal phase is calculated relative to the  $M_2$  tidal period (12.42 h). The reference for zero phase is arbitrary, but roughly coincides with the minimum in  $M_2$  surface displacement. It is important to note that the 9 day time period is insufficient to average out the predominantly  $M_2$  tidal signal in the diurnal ensemble average. Roughly 49% of the  $M_2$  signal is still retained after diurnal averaging over the observational period. On the other hand, over 16  $M_2$  cycles are completed within the 9 day window, so that the diurnal band is much more cleanly averaged out from the tidal ensemble average, with only 6% of the diurnal signal remaining.

The ensemble averages for 300 and 1200 kHz observations appear to suggest diurnal patterns (Figures 3c and 3e) with weak  $M_2$  tidal variations (Figures 3d and 3f). The ADCP backscatter diurnal and tidal patterns did not show significant variability with depth. The 24 h period, which appears most clearly in the 300 kHz data (Figure 3e), can be associated with both tidal and insolation forcing. The time of day average for  $\hat{S}_{v,1200}$  (Figure 3c) shows stronger semidiurnal variation with peaks near dawn and dusk, although this is not apparent in the  $M_2$  average. Although the diurnal band is not well resolved, dominantly semidiurnal tidal amplitude and currents during the study period indicate that the diurnal 300 and 1200 kHz variations are more likely associated with solar driven diel biological responses. The weak variations with  $M_2$  phase for both frequencies further supports this interpretation.

Backscatter at 6 MHz shows variability in both ensemble averages. The relatively tighter scatter in the tidal band, along with the fact that the influence of the diurnal band is weak on the tidal average, suggests that variations at the higher acoustic frequency are dominantly tidal. In other words, the apparent diurnal variability in Figure 3a is largely an artifact of the short averaging window. Optical backscatter closely tracked the high-frequency acoustic backscatter. Ensemble averages for optical properties are not considered robust, however, due to the shorter sampling periods so these are not presented. Instead, we will examine the correlations between optical and acoustical backscatter further below.

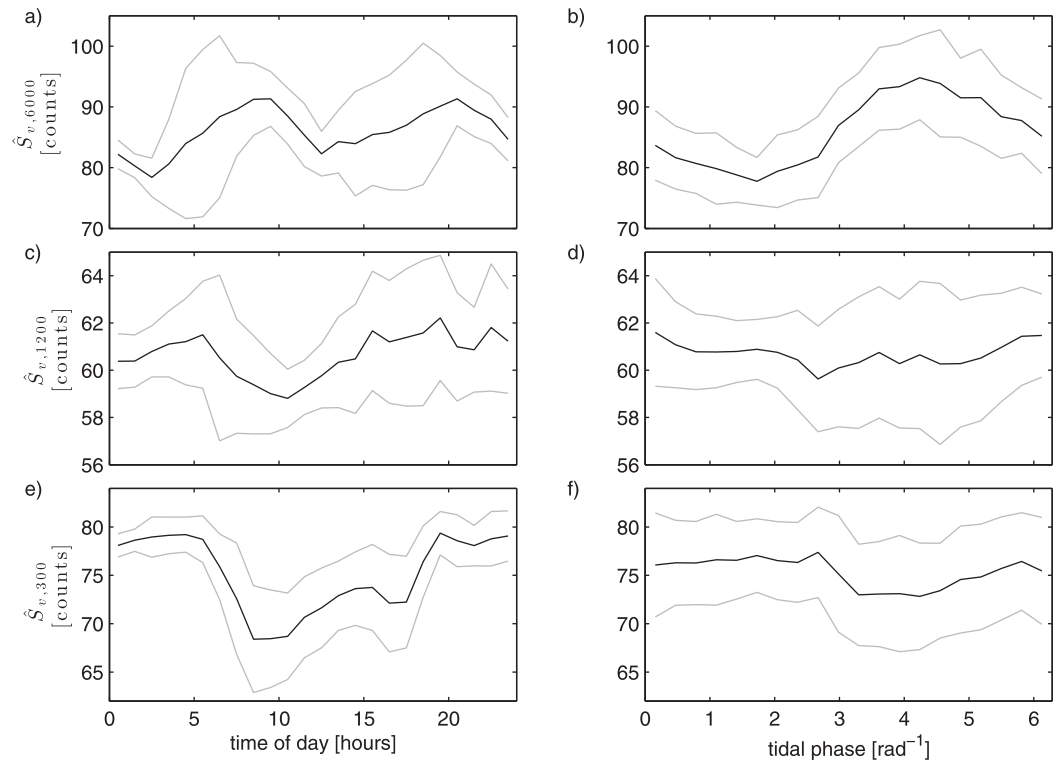


**Figure 3.** Ensemble-averaged acoustic backscatter at (a and b) 6 MHz (c and d) 1200 kHz, and (e and f) 300 kHz as a function of (left) time of day and (right)  $M_2$  tidal phase. Gray lines represent one standard deviation in the observational data.

The variation in  $\hat{S}_{v,6000}$  with wave height (9 m ADCP) is shown in Figure 4 with depth-averaged cross-shore currents as measured by the 9 m ADCP shown in color. Values for  $\hat{S}_{v,6000}$  show a clear increase for higher wave heights although overall correlation with  $H_{1/3}$  is weak ( $R^2=0.28$ ). The data point toward a significant relation with cross-shore flow, with high  $\hat{S}_{v,6000}$  coinciding with offshore currents, indicative of a scatterer source on the shallow reef flat. The variation in  $\hat{S}_{v,6000}$  with  $H_{1/3}$  is much more apparent if we examine the fit separately for positive and negative cross-shore velocities, excluding very low magnitudes ( $<0.03 \text{ m s}^{-1}$ )

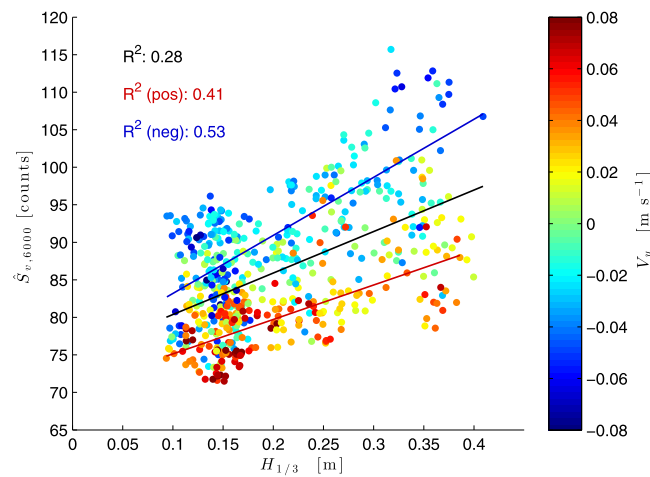


**Figure 4.**  $\hat{S}_{v,6000}$  vs significant wave height ( $H_{1/3}$ ). Cross-shore current velocity ( $V_y$ ) is shown in color. Solid lines represent least squares fits with  $R^2$  values as shown. Red and blue lines indicate least squares fits for positive ( $V_y > 0.03 \text{ m s}^{-1}$ , 40 min lag) and negative ( $V_y < 0.03 \text{ m s}^{-1}$ , 40 min lag) cross-shore velocities, respectively.

to distinguish the two limits more clearly. For offshore directed flow, the relationship improves to  $R^2=0.53$ .

For the full data set, a linear fit for  $\hat{S}_{v,6000}$  with cross-shore velocity at the 9 m ADCP gives  $R^2=0.28$ . The correlation with cross-shore velocity is improved by lagging  $\hat{S}_{v,6000}$  in time, increasing to 0.39 with a 40 min lag, consistent with scatterers advected from a remote location. The principal variability in the 20 min averaged currents is associated with semidiurnal tidally driven flow (Figures 2g and 2h), so the correlation for  $\hat{S}_{v,6000}$  with cross-shore flow is consistent with the tidal dependence apparent in the ensemble average in Figure 3b. Variations for  $\hat{S}_{v,6000}$  with alongshore (x) flow were notably weaker ( $R^2=0.09$ ), with slightly



higher  $\hat{S}_{v,6000}$  values associated with SW directed flow. Relationships are similar using velocities at the 12 m ADV spar.

If we consider the effect of waves and apply the fit between  $\hat{S}_{v,6000}$  and  $V_y$  separately for high ( $>0.3$  m) and low ( $<0.15$  m) wave conditions, the correlation improves significantly, with  $R^2$  values of 0.51 and 0.37, respectively. With a 40 min lag, the linear fit improves further to 0.63 and 0.58, for high and low wave conditions, respectively. The effect of a lag in the 6 MHz ABS data on the correlations with wave height is negligible, reflecting the much longer time scales associated with changes in wave forcing.

Low-frequency backscatter,  $\hat{S}_{v,300}$ , did not indicate significant relationships with wave height or current directions, consistent with a diurnal dependence. Backscatter at 1200 kHz shows an apparent correlation with cross-shore flow for high wave conditions with  $R^2=0.55$ , with higher  $\hat{S}_{v,1200}$  for offshore flow. Closer examination revealed this to be an artifact associated with the phase relation between the  $M_2$  cycle and time of day, where offshore currents coincided with the semidiurnal dawn/dusk peaks in  $\hat{S}_{v,1200}$  during the high wave event. The correlation weakens and changes sign over the course of the week as offshore currents shifted in phase relative to the diurnal cycle. The transient correlation is not apparent for  $\hat{S}_{v,300}$  where variability occurs at longer diurnal scales.

As noted earlier, the shorter optical data time series preclude reliable correlations with forcing. We can shed some light on the mechanisms driving variations in optical properties by examining the relationships between optical and acoustic data, however. No significant relationships were noted between optical properties and  $\hat{S}_{v,300}$  or  $\hat{S}_{v,1200}$ . Optical data were strongly correlated with higher-frequency ABS, however, as illustrated in Figure 5. The variations in optical backscatter at 532 nm (green) had  $R^2=0.79$  (Figure 5a) with similar relationships at 470 nm (blue) and 650 nm (red) (0.79 and 0.83, respectively). The optical backscatter ratio  $b_b/b$  (Figure 5b) also shows a high correlation, although the relationship is modulated by wave height.

Backscatter ratio has been related to the bulk refractive index  $n$  of suspended particulate matter [Brown and Gordon, 1974] and is thus influenced by the relative contributions from phytoplankton, which have low  $n$ , and inorganic particles, with higher values of  $n$  [Boss et al., 2004]. Chlorophyll concentrations normalized by beam attenuation  $c$  were shown by Boss et al. [2004] to be inversely related to backscatter ratio for a coastal shelf environment, reflecting the effects of varying  $n$ . In addition, the backscatter ratio has also been shown to be dependent on the particle-size distribution, specifically on the relative proportion of small to large particles [Ulloa et al., 1994]. Twardowski et al. [2001] related the backscatter ratio to the slope of a Junge-type distribution with a positive relationship between the Junge distribution exponent  $\zeta$  and the backscatter ratio, for  $\zeta$  greater than about 3.2.

Following Boss et al. [2004], we examine the relationship between backscatter ratio and the ratio of chlorophyll concentration to attenuation  $[chl]/c$  in Figure 6. For the overall data set, the correlation is very weak. A much clearer relationship is evident within wave height bands, with a strong negative correlation ( $R^2=0.68$  for  $H_{1/3} > 0.35$ ). The slope for the linear relationship in each wave height band is similar to that in the relationship observed by Boss et al. [2004] with a vertical offset that increases with  $H_{1/3}$ . For a selected wave

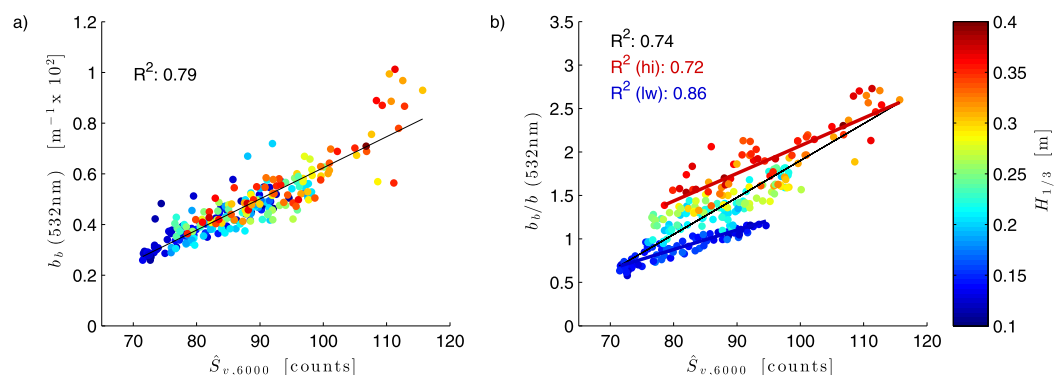


**Figure 5.** (a) Optical backscatter and (b) optical backscatter ratio at 532 nm versus 6 MHz ABS. Wave height is shown in color in both plots, as indicated by the scale at left. Solid lines represent least squares fits with  $R^2$  values as shown. For Figure 5b, red and blue lines indicate least squares fits for high ( $H_{1/3} > 0.3$  m) and low ( $H_{1/3} < 0.15$  m) wave conditions, respectively.

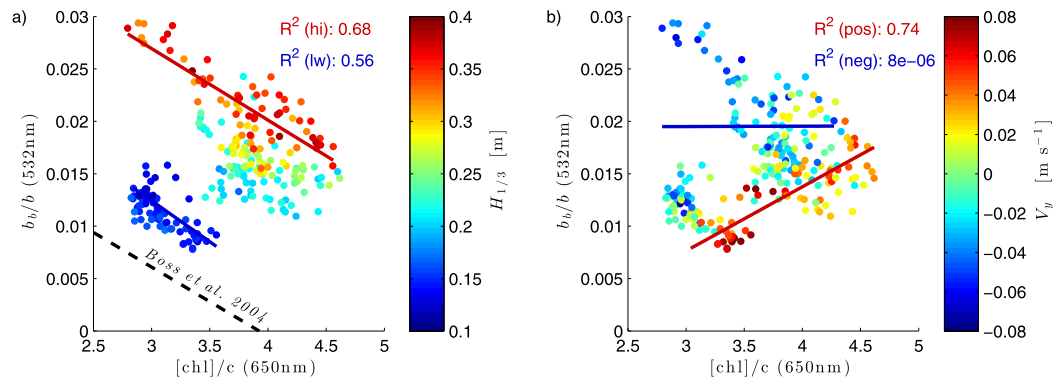


**Figure 6.** Optical backscatter ratio ( $b_b/b$ ) at 532 nm versus ratio of chlorophyll to attenuation ( $c$ ) at 650 nm with (a) wave height and (b) cross-shore velocity indicated by color. Red and blue lines in Figure 6a represent linear regressions for high ( $H_{1/3} > 0.3$  m) and low ( $H_{1/3} < 0.15$  m) wave height bands, respectively. Dashed black line indicates the fit observed by Boss *et al.* [2004]. Red and blue lines in Figure 6b indicate regressions for positive ( $V_y > 0.03$  m s<sup>-1</sup>, 40 min lag) and negative ( $V_y < 0.03$  m s<sup>-1</sup>, 40 min lag) cross-shore velocities, respectively.

height, the variations in backscatter ratio are thus consistent with variations in relative phytoplankton concentrations. Changes in  $b_b/b$  that deviate from the Boss *et al.* [2004] fit can then be associated with variations in particle-size distributions, with higher backscatter ratio corresponding to an increase in relative proportion of smaller particles. If the particle-size distribution here were Jungian with  $\zeta > 3.2$ , then the increase in backscatter ratio with wave height evident in Figures 5b and 6a would be consistent with an increase in relative concentration of small particles and thus an increase in size distribution slope  $\zeta$ .

Figure 6b highlights the role of the cross-shore current in the optical variations. For a set wave height, changes in  $b_b/b$  correspond to variations in cross-shore flow, such that offshore flow results in lower  $[chl]/c$  and higher  $b_b/b$ , consistent with increasing inorganic particle content (relative to phytoplankton). Although chlorophyll content decreases with offshore flow (not shown), variations within wave height bands are relatively weak. The variations in  $[chl]/c$  within a wave band are instead associated with increases in  $c$  for offshore directed flow, described further below, suggesting an increase in total particulate matter. This interpretation is further substantiated by the increase in acoustic backscatter with offshore flow as shown in Figure 4. The close relationship between  $\hat{S}_{v,6000}$  and optical backscatter, apparent in Figure 5, implies a similar optical response. For onshore directed flow,  $[chl]/c$  shows a fairly tight relation with a trend that diverges nearly orthogonally from the Boss *et al.* [2004] fit (Figure 6b). Following the discussion above, we can interpret this variation as associated with changes in the particle-size distribution. The offset in the relations between  $\hat{S}_{v,6000}$  and  $b_b/b$  within wave height bands apparent in Figure 5 can thus similarly be interpreted in terms of changes in particle sizes.

The changes in particle-size distribution implied by the relationship between  $[chl]/c$  and  $b_b/b$  in Figure 6b for onshore directed flow indicate that offshore conditions are also varying with changing wave height. This

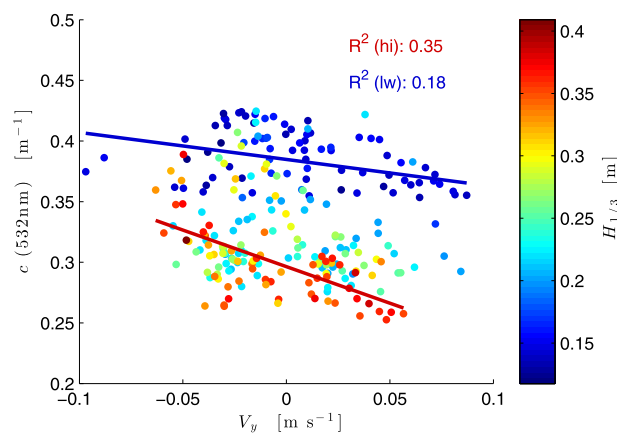


**Figure 7.** Optical attenuation at 532 nm versus cross-shore velocity, with significant wave height in color.

suggests that some fraction of the onshore flow has a recent shoreward history and that suspension times for particulate matter are longer than the tidal cycles. The relatively rapid relaxation (over a few days) of the between the high and low wave regimes in Figure 6a, on the other hand, provide an upper limit for suspension and/or residence times.

While the changes in  $b_b/b$  can be accounted for by variations in  $[chl]/c$  and particle-size distribution, changes in attenuation  $c$  (Figure 7) are less intuitive. Attenuation is largely determined by total scatter,  $b$ , so these are closely correlated, with both quantities showing a negative

correlation with wave height. Together with the increase in optical backscatter with wave height, this relationship drives the observed increase in backscatter ratio. For the full data set, attenuation shows a weak relationship with cross-shore current. A negative correlation is apparent within wave height bands, however, with increased attenuation for offshore directed flow. This correlation largely drives the variations in  $[chl]/c$  evident in Figure 6 within wave height bands. The variations in  $c$  are relatively small ( $\sigma=0.047\text{ m}^{-1}$  at  $\lambda = 532\text{ nm}$ ) for the data set. The changes with wave height are likely associated with the effect of the particle-size distribution on the attenuation. For constant index of refraction, spectral attenuation is expected to diminish with increasing Junge exponent  $\zeta$  [Diehl and Haardt, 1980; Boss *et al.*, 2001]. A change in the particle-size distribution toward greater numbers of smaller particles would thus result in a reduction in total attenuation. The fact that optical and acoustic backscatter increase would require that both backscatter quantities respond similarly to the changes in particle-size distribution.

The observations then point toward an overall picture where an increase in wave height introduces a supply of fine particles. This leads to a shift in the particle-size distribution such that backscatter increases, while total scatter (and attenuation) decrease slightly. For a set wave height (and corresponding particle-size distribution), variations in backscatter ratio and attenuation are due to changes in cross-shore flow that introduce variations in relative inorganic contributions, along with slightly higher chlorophyll content for onshore directed flow. Generally weak changes in chlorophyll indicate a lack of wave influence on primary production for this location and study period.

The increase in attenuation with offshore flow that is apparent for larger wave conditions (Figure 7) points to an increase in total particulate matter for flow coming off of the reef flat, consistent with a shoreward source for small particles. For larger waves, this also results in a larger spread in  $[chl]/c$  and accounts for the weak relationship between  $b_b/b$  and  $[chl]/c$  for offshore flow in Figure 6b. For onshore directed flow, the variations in  $b_b/b$  with  $[chl]/c$  are associated with reduced scatter as wave height increases, presumably associated with variations in particle-size distributions.

#### 4. Optical Model

The light field throughout the water column was modeled using the HydroLight v. 5.2 RTE model [Mobley and Sundman, 2001]. The model was set up to provide full spectral output (390–710 nm) at 20 nm resolution. Depth resolution was 0.25 m over the 9 m water column above the sensors. The measured coefficients of total  $a$ ,  $c$ , and  $b_b$  were used as inputs and were assumed uniform throughout the water column. Pure water absorption and scattering coefficients were used from Smith *et al.* [1981]. The input for bottom reflectance was dependent on the measured distribution of sand cover to coral cover (30:70 ratio) with the standard reflectance spectra available in HydroLight. As the interest was in examining the variability within the water column over time, a constant incoming light field with zero cloud cover was assumed for estimation of the remote sensing reflectance,  $R_{rs}$ . Figure 8a shows the resultant mean  $R_{rs}$  signal over the deployment with up to 40% variability in the signal indicating significant influence of optical constituents in the water column.

In an effort to evaluate the constituent(s) responsible for the variability in  $R_{rs}$  during the experiment, the minimum  $R_{rs}$  spectra were subtracted from the maximum. The resulting spectra were found to be elevated in the green and especially the blue wavelengths (Figure 8b). Peak reflectance was at 490 nm with distinct peaks at 530 and 570 nm. The spectra also suggested limited contributions from biogenic sources such as a dissolved optical signature (i.e., CDOM) and chlorophyll, which would have shown significantly more absorption and decreased reflection in the blue. The difference spectral signature was found to be nearly identical to that found by Dierssen *et al.* [2009] during a whitening event in the Bahamas (Figure 8b) where the  $R_{rs}$  was found to be caused by inorganic particles consistent with (micron-sized) aragonite particles. Relevant to this study, Dierssen *et al.* [2009] found that the backscattering ratio provided additional information about the composition of particles suspended in the water column, particularly the amount of inorganic materials (i.e., suspended sediments) with a high refractive index relative to water [Ulloa *et al.*, 1994; Twardowski *et al.*, 2001]. The maximum value for  $b_b/b$  of 3% in this study was about half the maximum in Dierssen *et al.* [2009], but was, however, consistent with the average values. Analysis of suspended particles filtered from whittings [Shinn *et al.*, 1989] identified nonspherical needles with 0.25  $\mu\text{m}$  widths and lengths of 2–3  $\mu\text{m}$  as well as aggregates of these needles with scales of 10–15  $\mu\text{m}$ . These deviations from sphericity

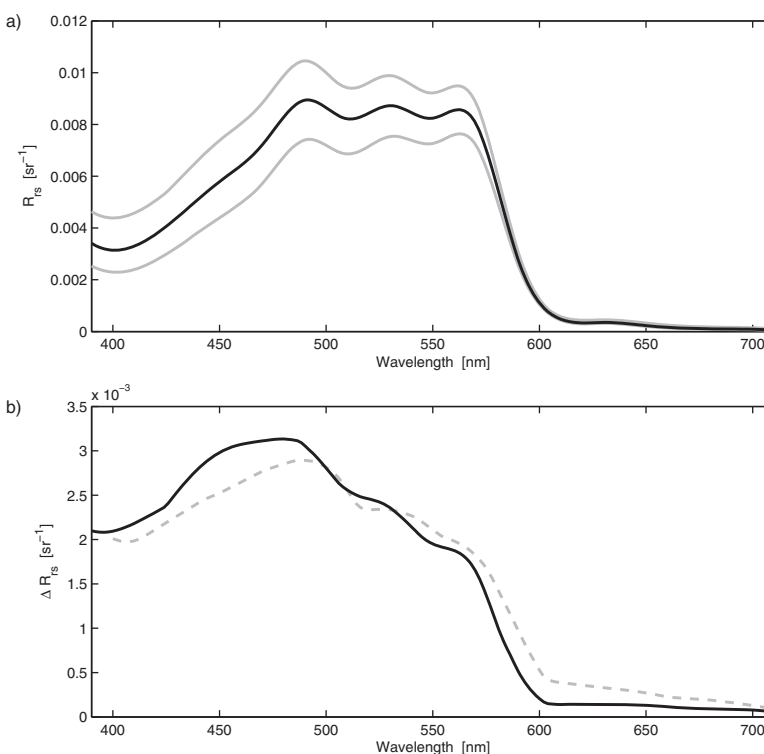


**Figure 8.** (a) Remote sensing reflectance spectra ( $R_{rs}$ ) from Hydrolight analysis. Maximum and minimum values are shown in gray. (b) Difference in maximum, minimum  $R_{rs}$  versus wavelength. Spectral signature for whitening events from Dierssen *et al.* [2009] is shown in dashed gray for comparison.

generally serve to enhance the backscattering ratio [Clavano *et al.*, 2007]. It also been documented that these particles can also show a spectral dependency (enhanced in the blue) [Dierssen *et al.*, 2009; McKee and Cunningham, 2005] and have been attributed to different modes of particles when the particle-size distribution does not closely follow a Jungian or power-law distribution.

## 5. Discussion and Conclusions

Observations and analysis indicate that the optical characteristics for a tropical forereef environment are primarily determined by a combination of wave conditions and cross-shore flow velocity for the study period. Optical backscatter is closely correlated with high-frequency acoustic backscatter (Figure 5a) and both increase with increasing wave energy and offshore directed flow (Figure 4). The variation in optical backscatter ratio relative to  $[chl]/c$  (Figure 6a) within wave height bands closely follows the fit obtained by Boss *et al.* [2004], which corresponds to variations in the relative inorganic load. Inorganic content is thus largely determined by cross-shore flow.

As wave height increases, both  $b_b$  and  $\hat{S}_{v,6000}$  increase, while total optical scatter decreases. The backscattering ratio continues to follow the slope of the Boss *et al.* [2004] fit, but with a vertical offset. Both of these observations are consistent with changing particle-size distribution, with a relative increase in small particles. The concurrent decreases in total scatter and attenuation imply that there is an increase in smaller particles with a concurrent decrease in larger particles, since increases in the larger particle classes within the optically and acoustically relevant ranges would lead to increases in scattering and attenuation.

The decrease in total optical scattering,  $c$ , with increasing wave forcing is consistent with increases in relative concentrations of small particles and associated steepening in the particle-size distribution. The dependence on flow direction points toward a shoreward source and wave-driven resuspension, although aggregate breakup may also play a role. Suspended particles in the coastal ocean often exist in aggregated states as “flocs” [Gibbs, 1987]. Optical and acoustical signatures are associated with floc size rather than constituent particles [Vincent and MacDonald, 2015]. Breakup of flocs due to increased wave breaking on the

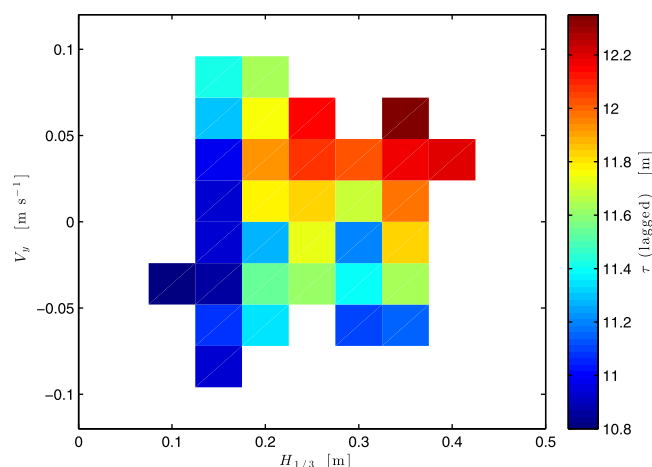


**Figure 9.** Bin averaged optical attenuation depth ( $\tau$ , lagged by 40 min) versus cross-shore velocity (vertical axis) and significant wave height (horizontal axis).

reef top could then result in a shift in effective particle-size distribution. Indeed *Gibbs and Wolanski* [1992] found that optical backscatter increased while floc size decreased with increasing flow energy in laboratory channel experiments. The increase in fine particles with increasing wave height can alternately be attributed to increased resuspension or to break up of flocs or, most likely, some combination of the two.

The analysis here is based on measurements at a single location, which inevitably presents some limits on our ability to generalize results, particularly within spatially complex reef environments. The measurement site is representative of a typical forereef environment, how-

ever, with bathymetry that is relatively uniform alongshore over the tidal excursion length ( $\sim \pm 0.5$  km). The cross-shore excursion (also  $\pm 0.5$  km) spans the full forereef environment depth profile from deep offshore to the shallow reef top, without notable variations. High-frequency acoustic backscatter,  $\hat{S}_{v,6000}$ , showed no significant dependence on alongshore flow further supporting the local, 2-D cross-shore interpretation. The lack of a CDOM signature in the optical reflectance spectral data indicates minimal influence from organic sources.

It is important to note that the analysis and interpretations here have focused on the influence of wave and tidal forcing in determining optical and acoustical properties in a quasi-steady manner. The hypothesis of floc breakup assumes that flocs exist at low wave conditions, preceding high wave conditions. The observational time period considered here, however, began with larger wave conditions which diminished over the time period. The quasi-steady assumption therefore, neglects possible effects of hysteresis, associated with biological effects on aggregate formation, for example.

The correlated backscatter response between the optics and the high-frequency acoustics across the observations (Figure 5a) would suggest that both have similar responses across the varying particle-size distributions. Analysis of optical backscattering efficiency by *Clavano et al.* [2007] shows relatively uniform backscatter response for inorganic spheroidal particles within the 6 MHz acoustic geometric scattering regime ( $>40 \mu\text{m}$ ). Alternately, both optics and acoustics exhibit diminishing efficiencies for particles smaller than about  $5 \mu\text{m}$ . The linear correlation in Figure 5a further requires that backscattering efficiency decay rates match, however, pointing toward scatterers in the larger classes. If particles are assumed to be similar to those previously observed for whittings [*Shinn et al.*, 1989], the observations would require scatterers for the 6 MHz acoustics and the optics that are primarily in aggregate states, consistent with the samples analyzed in *Dierssen et al.* [2009]. While particle sampling during this study would have been useful in elucidating their dynamics, it is clear that this setting is complex and that both particle size and composition (organic/inorganic) is changing over time scales of days and dependent on the physical forcing. The issue of aggregation also makes it imperative that sampling approaches be nondestructive (i.e., imaging) to maintain their in situ conformations and optical and acoustical cross sections.

Acoustic backscatter at 300 kHz showed a diurnal response with no notable correlation with wave conditions. The 1200 kHz data varied on a semidiurnal period, with peaks near dawn and dusk. Although the diurnal cycle was not well-resolved with the relatively short study period, these observations would suggest a biological origin for scatterers, likely zooplankton with scales comparable to the acoustic wavelengths. The lack of correlation with the optical properties indicates that these larger scatterer classes would not have a discernible optical signature for conditions comparable to those during the study period.

The variations in optical water properties have implications for light properties in the water column and for remote sensing. This is manifested in variations in the first optical depth, defined as  $\tau = 1/K_d$ , where  $K_d$  is the



diffuse attenuation coefficient, calculated using Hydrolight and assumed here to be constant over the water column. The attenuation depth represents the depth that accounts for 90% of the diffusely reflected light [Smith and Baker, 1978]. Values for  $\tau$ , lagged by 40 min to account for advection, were binned versus cross-shore velocity and significant wave height (Figure 9). The diffuse attenuation coefficient is largely determined by changes in absorption,  $a$  [Mobley, 1994], which varies similarly to total attenuation  $c$  (Figure 7). The binned data show deeper optical penetration (greater  $\tau$ ) for onshore directed flow combined with higher wave conditions, where relative concentrations of small particle concentrations increase (large waves) while overall inorganic loads decrease (onshore flow). It remains unclear whether the observed (and somewhat counterintuitive) increase in optical penetration for higher wave conditions will persist as wave height increases further. We can speculate that as wave forcing increases, at some point, the influence of increased particle load will overwhelm the effects of the shift to smaller particle sizes.

Relevant to this study is the potential for particles and hydrodynamic processes to be remotely sensed. With a specific particle signature shown to be remotely identifiable [see Dierssen *et al.*, 2009], spatially heterogeneous particle distributions may be indicative of hydrodynamic conditions and/or processes that have been shown to modify acoustical and optical properties in this study (i.e., tidal currents and wave heights). While in situ measurements provide a detailed view of these processes in a given location, this optical signature may provide a larger field view, especially given the increased spectral and temporal (i.e., geostationary) capabilities of remote sensing platforms [Andréfouët *et al.*, 2013].

#### Acknowledgments

The work presented here was carried out with funding from the Office of Naval Research under awards N00014-12-1-0221, N00014-15-1-2304 and N00014-13-1-0340. We are grateful to Chris Colgrove, Ian Robbins, and Mathew Mesubed who assisted with the field deployments, and to Lori Colin and the CRRF staff for their expert assistance with all of the operations. The data presented are available by contacting G. Pawlak (pawlak@ucsd.edu).

#### References

- Andréfouët, S., M. M. M. Guillaume, A. Delval, F. M. A. Rasoamanendrika, J. Blanchot, and J. H. Bruggemann (2013), Fifty years of changes in reef flat habitats of the Grand Récif of Toliara (SW Madagascar) and the impact of gleaning, *Coral Reefs*, 32, 757–768, doi:10.1007/s00338-013-1026-0.
- Blondeau-Patissier, D., V. Brando, K. Oubelkheir, A. Dekker, L. Clementson, and P. Daniel (2009), Bio-optical variability of the absorption and scattering properties of the Queensland inshore and reef waters, Australia, *J. Geophys. Res.*, 114, C05003, doi:10.1029/2008/JC005039.
- Boss, E., W. S. Pegau, W. D. Gardner, J. R. V. Zaneveld, A. H. Barnard, M. S. Twardowski, G. C. Chang, and T. D. Dickey (2001), Spectral particulate attenuation and particle size distribution in the bottom boundary layer of a continental shelf, *J. Geophys. Res.*, 106(C5), 9509–9516.
- Boss, E., W. S. Pegau, M. M. Lee, M. Twardowski, E. Shybanov, G. Korotaev, and F. Baratange (2004), Particulate backscattering ratio at LEO 15 and its use to study particle composition and distribution, *J. Geophys. Res.*, 109, C01014, doi:10.1029/2002JC001514.
- Boss, E., R. Collier, G. Larson, K. Fennel, and W. S. Pegau (2007), Measurements of spectral optical properties and their relation to biogeochemical variables and processes in Crater Lake National Park, OR, *Hydrobiologia*, 574, 149–159.
- Brown, O. B., and H. R. Gordon (1974), Size-refractive index distribution of clear coastal water particulates from light scattering, *Appl. Opt.*, 13(12), 2874–2881.
- Clavano, W. R., E. Boss, and L. Karp-Boss (2007), Inherent optical properties of non-spherical marine-like particles: From theory to observations, *Oceanogr. Mar. Biol.*, 45, 1–38.
- Colin, P. L. (2009), *Marine Environments of Palau*, Indo-Pacific Press, San Diego, Calif.
- Davis, R. F., C. C. Moore, J. R. V. Zaneveld, and J. M. Napp (1997), Reducing the effects of fouling on chlorophyll estimates derived from long-term deployments of optical instruments, *J. Geophys. Res.*, 102(C3), 5851–5855.
- Deines, K. L. (1999), Backscatter estimation using broadband acoustic Doppler current profilers, in *Proceedings of the IEEE Sixth Working Conference on Current Measurement*, pp. 249–253, IEEE.
- Diehl, P., and H. Haardt (1980), Measurement of the spectral attenuation to support biological-research in a plankton tube experiment, *Oceanol. Acta*, 3(1), 89–96.
- Dierssen, H. M., R. C. Zimmerman, and D. J. Burdige (2009), Optics and remote sensing of Bahamian carbonate sediment whittings and potential relationship to wind-driven Langmuir circulation, *Biogeosciences*, 6, 487–500.
- Fortes, M. (2000), The effects of siltation on tropical coastal ecosystems, in *Oceanographic Processes of Coral Reefs*, edited by E. Wolanski, pp. 93–112, CRC Press, Boca Raton, Fla.
- Gibbs, R. J. (1987), Sources of estuarine sediments and their coagulation, in *Sedimentation Control to Reduce Maintenance of Dredging of Navigational Facilities in Estuaries*, pp. 32–52, Natl. Res. Council, Natl. Acad. Press, Washington D. C.
- Gibbs, R. J., and E. Wolanski (1992), The effect of flocs on optical backscattering measurements of suspended material concentration, *Mari. Geol.*, 107(4), 289–291.
- Gove, J. M., G. J. Williams, M. A. McManus, S. F. Heron, S. A. Sandin, O. J. Vetter, and D. G. Foley (2013), Quantifying climatological ranges and anomalies for Pacific coral reef ecosystems, *PLoS One*, 8(4), e61974.
- Hay, A. E. (1991), Sound scattering from a particle-laden, turbulent jet, *J. Acoust. Soc. Am.*, 90(4), 2055–2074.
- Hedley, J., et al. (2016), Remote sensing of coral reefs for monitoring and management: A review, *Remote Sens.*, 8(2), 118.
- Holden, H., and E. LeDrew (2002), Measuring and modeling water column effects on hyperspectral reflectance in a coral reef environment, *Remote Sens. Environ.*, 81(2), 300–308.
- Jouan, A., S. Ouillet, P. Douillet, J. P. Lefebvre, J. M. Fernandez, X. Mari, and J. M. Froidefond (2008), Spatiotemporal variability in suspended particulate matter concentration and size distribution in a coral reef lagoon, *Mar. Geol.*, 256, 36–48.
- Larcombe, P., P. V. Ridd, A. Prytz, and B. Wilson (1995), Factors controlling suspended sediment on inner-shelf coral reefs, Townsville, Australia, *Coral Reefs*, 14(3), 163–171.
- Lynch, J. F., G. T. F., C. R. Sherwood, J. D. Irish, and B. H. Brumley (1997), Acoustical and optical backscatter measurements of sediment transport in the 1988–1989 STRESS experiment, *Cont. Shelf Res.*, 17(4), 337–366.
- McKee, D., and A. Cunningham (2005), Evidence for wavelength dependence of the scattering phase function and its implication for modeling radiance transfer in shelf seas, *Appl. Opt.*, 44(1), 126–135.

- Medwin, H., and C. S. Clay (1997), *Fundamentals of Acoustical Oceanography*, Academic.
- Minghelli-Roman, A., and C. Dupouy (2014), Correction of the water column attenuation: Application to the seabed mapping of the lagoon of new Caledonia using MERIS images, *IEEE J. Sel. Top. Appl. Earth Observ. Remote Sens.*, 7(6), 2619–2629.
- Mishra, D., S. Narumalani, D. Rundquist, and M. Lawson (2006), Benthic habitat mapping in tropical marine environments using quickbird multispectral data, *Photogramm. Eng. Remote Sens.*, 72(9), 1037–1048.
- Mobley, C. D. (1994), *Light and Water: Radiative Transfer in Natural Waters*, Academic.
- Mobley, C. D., and L. K. Sundman (2001), *HYDROLIGHT 4.2, Users' Guide*, Sequoia Sci., Redmond, Wash.
- Molina, L., G. Pawlak, J. R. Wells, S. G. Monismith, and M. A. Merrifield (2014), Diurnal cross-shore thermal exchange on a tropical foreereef, *J. Geophys. Res. Oceans*, 119, 6101–6120, doi:10.1002/2013JC009621.
- Monismith, S. G., A. Genin, M. Reidenbach, G. Yahel, and J. Koseff (2006), Thermally driven exchanges between a coral reef and the adjoining ocean, *J. Phys. Oceanogr.*, 36, 1332–1347.
- Moore, C., M. S. Twardowski, and J. R. V. Zaneveld (2000), The ECO VSF-A multi-angle scattering sensor for determination of the volume scattering function in the backward direction, *Proc. Ocean Optics XV*, Monaco, edited by S. G. Ackleson and J. Marra, SPIE.
- Morimoto, N., Y. Furushima, M. Nagao, T. Irie, A. Iguchi, A. Suzuki, and K. Sakai (2010), Water-quality variables across Sekisei reef, a large reef complex in southwestern Japan, *Pacific Sci.*, 64(1), 113–123.
- Mumby, P. J., W. Skirving, A. E. Strong, J. T. Hardy, E. F. LeDrew, E. J. Hochberg, R. P. Stumpf, and L. T. David (2004), Remote sensing of coral reefs and their physical environment, *Mar. Pollut. Bull.*, 48(3), 219–228.
- Pegau, W., D. Gray, and J. Zaneveld (1997), Absorption and attenuation of visible and near-infrared light in water: Dependence on temperature and salinity, *Appl. Opt.*, 36, 6035–6046.
- Presto, M. K., A. S. Ogston, C. D. Storlazzi, and M. E. Field (2006), Temporal and spatial variability in the flow and dispersal of suspended sediment on a fringing reef flat, Molokai, Hawaii, *Estuarine Coastal Shelf Sci.*, 67(1), 67–81.
- Sevadjian, J., M. A. McManus, and G. Pawlak (2010), Effects of physical structure and processes on thin zooplankton layers in Mamala Bay, Hawai'i, *Mar. Ecol. Prog. Ser.*, 409, 95–106.
- Shinn, E. A., R. P. Steinen, B. H. Lidz, and P. K. Swart (1989), Whitings, a sedimentologic dilemma: Perspectives, *J. Sediment. Res.*, 59(1), 147–161.
- Smith, R. C., and K. S. Baker (1978), The bio-optical state of ocean waters and remote sensing, *Limnol. Oceanogr.*, 23(2), 247–259.
- Smith, R. C., and K. S. Baker (1981), Optical properties of the clearest natural waters (200–800 nm), *Applied optics*, 20(2), 177–184.
- Storlazzi, C. D., and B. E. Jaffe (2008), The relative contribution of processes driving variability in flow, shear and turbidity over a fringing coral reef: West Maui, Hawaii, *Estuarine Coastal Shelf Sci.*, 77, 549–564.
- Storlazzi, C. D., A. S. Ogston, M. H. Bothner, M. E. Field, and M. K. Presto (2004), Wave-and tidally-driven flow and sediment flux across a fringing coral reef: Southern Molokai, Hawaii, *Cont. Shelf Res.*, 24(12), 1397–1419.
- Storlazzi, C. D., M. E. Field, M. H. Bothner, M. K. Presto, and A. E. Draut (2009), Sedimentation processes in a coral reef embayment; Hanalei Bay, Kauai, *Mar. Geol.*, 264(3), 140–151.
- Stumpf, R. P., K. Holderied, and M. Sinclair (2003), Determination of water depth with high-resolution satellite imagery over variable bottom types, *Limnol. Oceanogr.*, 48(1, Part 2), 547–556.
- Twardowski, M. S., J. M. Sullivan, P. L. Donaghay, and J. R. V. Zaneveld (1999), Microscale quantification of the absorption by dissolved and particulate material in coastal waters with an ac-9, *J. Atmos. Oceanic Technol.*, 16, 691–707.
- Twardowski, M. S., E. Boss, J. B. Macdonald, W. S. Pegau, A. H. Barnard, and J. R. V. Zaneveld (2001), A model for estimating bulk refractive index from the optical backscattering ratio and the implications for understanding particle composition in case I and case II waters, *J. Geophys. Res.*, 106(C7), 14,129–14,142.
- Ulloa, O., S. Sathyendranath, and T. Platt (1994), Effect of the particle-size distribution on the backscattering ratio in seawater, *Appl. Opt.*, 33(30), 7070–7077.
- Vincent, C. E., and T. MacDonald (2015), A flocculi model for the acoustic scattering from flocs, *Cont. Shelf Res.*, 104, 15–24.
- Weber, M., D. de Beer, C. Lott, L. Polerecky, K. Kohls, R. M. Abed, T. G. Ferdeman, and K. E. Fabricius (2012), Mechanisms of damage to corals exposed to sedimentation, *Proc. Natl. Acad. Sci. U. S. A.*, 109(24), E1558–E1567.
- Wells, J., J. P. Fram, and G. Pawlak (2012), Solar warming of near bottom water over a fringing reef, *J. Mar. Res.*, 70, 641–660.
- Whitmire, A. L., E. Boss, T. J. Cowles, and W. S. Pegau (2007), Spectral variability of the particulate backscattering ratio, *Opt. Exp.*, 15, 7019–7031.
- Zaneveld, J. R. V., J. C. Kitchen, and C. M. Moore (1994), Scattering error correction of reflecting-tube absorption meters, *Proc SPIE Int. Soc. Opt. Eng.*, 2258, 44–55.